

Gram–Schmidt Orthogonalization for Rapid Reconstructions of Fourier Transform Infrared Spectroscopic Imaging Data

ROHIT BHARGAVA and IRA W. LEVIN*

Laboratory of Chemical Physics, NIDDK, National Institutes of Health, Bethesda, Maryland 20892-0520

Increasingly voluminous Fourier transform infrared (FT-IR) spectroscopic imaging data sets are being generated with the advent of both faster array detectors and the implementation of time-resolved imaging techniques, resulting in data processing becoming the limiting step in visualizing sample heterogeneity and temporal profile evolution. We report the application of a Gram–Schmidt vector orthogonalization procedure in interferogram space to provide a significant time saving advantage in processing of one to two orders of magnitude in comparison to conventional spectral processing. Illustrative data from human skin biopsies and from dynamic molecular reorganizations within liquid crystalline microdomains is employed to discuss the capabilities and limitations of this information-extraction approach.

Index Headings: Fourier transform infrared spectroscopy; FT-IR; Infrared spectroscopic imaging; Gram–Schmidt orthogonalization; Data processing; Skin; Time-resolved spectroscopy; Time-resolved imaging.

INTRODUCTION

An interferometer–focal plane array (FPA) detector combination¹ represents the instrumentation of choice to obtain infrared spectral data from extended sample areas under wavelength-limited spatial resolution conditions.² Large amounts of data, as for example, more than 10 megabytes per second, are routinely acquired in examining multiphase polymeric, biological, or inorganic materials. As opposed to optical microscopy, where spatial visualization is available instantaneously, the requirements for visualization of Fourier transform infrared (FT-IR) spectroscopic imaging data include Fourier transformation, ratio against an appropriate background data set, and baseline correction prior to constructing an image from the spatial distribution of the spectral absorbance of a specified chemical moiety. This time-consuming data processing requirement prevents the application of FT-IR spectroscopic imaging techniques in venues that require rapid responses, as for example, in process control units, in which infrequent sample anomalies appear.³ Thus, methods to spectroscopically identify sample heterogeneity without expending considerable time in processing large quantities of data would be helpful. Further, with the availability of fast detectors and improved protocols, real-time kinetics⁴ and time-resolved⁵ spectroscopic imaging applications are now feasible, resulting in complex spatio-temporal data sets that are tens of gigabytes in size. While data acquisition may require short time periods, the extraction of temporal absorbance profiles from an entire data set takes significantly longer. For example, a time-resolved experiment records 100 temporal reso-

lution elements in ~20 minutes, but data processing requires almost three hours before results can be accessed in terms of absorbance data. For these applications, a rapid visualization of the changes occurring within the sample would be helpful in validating experimental protocols and determining whether additional time should be devoted to further data processing.

The most expedient approach to image segmentation is to utilize a portion of the acquired interferogram which precludes Fourier transformation and results in a reduction in the dimensionality of the data set. It is well known that the overall blackbody curve is approximated by the centerburst of an interferogram, while the coarse structure of the absorbance spectrum is defined within a small region close to the centerburst of the interferogram. Thus, one approach to rapid processing may be to Fourier transform a small region around the centerburst and to examine the resulting low-resolution spectral profile. The same truncated interferogram, however, can also be employed for multivariate analysis without involving the computationally intensive transformations associated with FT methods by using a processing approach that is simple to implement and is computationally efficient. This approach involves a Gram–Schmidt (G-S) vector orthogonalization⁶ and has been previously employed in the interferogram domain for hybrid chromatography/infrared spectroscopic techniques,⁷ in the spectral domain for multivariate data processing,⁸ and in numerical transformations for magnetic resonance imaging (MRI) image analyses.⁹ While data orthogonalization is a primary step in many chemometric analyses, it is often accompanied by more complex computations. G-S orthogonalization of data, a particularly simple and direct approach, is often overlooked as a powerful data analysis tool. For IR absorption spectroscopy, a basis set consisting of background interferograms is established before initiating the experiment. This basis set is then used to detect the presence of infrared radiation absorbing species in real time by comparing the sample interferograms to the basis set. In this discussion, we present a data orthogonalization approach to rapidly extract information from spectroscopic imaging data sets from both static skin tissue biopsies and dynamic molecular reorganization studies.

GRAM–SCHMIDT VECTOR ORTHOGONALIZATION

The theory underlying the G-S orthogonalization process is well documented⁶ and additional considerations in an imaging context are briefly discussed next. Consider a series of interferograms in which each interferogram, I_k , consists of n sampling points each at optical retardations δ_m such that $m \leq n$ with some value h such that δ_n

Received 24 February 2004; accepted 21 April 2004.

* Author to whom correspondence should be sent.

= 0 and $h \leq n$. Alternately, each interferogram can be represented as a scalar associated with a unit vector of n dimensions, \mathbf{i}_k , given by

$$\mathbf{i}_k = \frac{\mathbf{I}_k}{\sqrt{\mathbf{I}_k^T \mathbf{I}_k}} \quad (1)$$

where the denominator is simply the scalar magnitude of \mathbf{I}_k . Any orthonormal vector to \mathbf{i}_k , \mathbf{i}_j , is then given by

$$\mathbf{i}_j = \frac{\mathbf{I}_j - (\mathbf{i}_k^T \mathbf{I}_j) \mathbf{i}_k}{\sqrt{[\mathbf{I}_j - (\mathbf{i}_k^T \mathbf{I}_j) \mathbf{i}_k]^T [\mathbf{I}_j - (\mathbf{i}_k^T \mathbf{I}_j) \mathbf{i}_k]}} \quad (2)$$

In this manner, p vectors may be employed to form a basis set of orthonormal (linearly independent) vectors given by

$$\mathbf{i}_p = \frac{\mathbf{I}_p - \sum_{k=1}^{p-1} (\mathbf{i}_k^T \mathbf{I}_p) \mathbf{i}_k}{\sqrt{[\mathbf{I}_p - \sum_{k=1}^{p-1} (\mathbf{i}_k^T \mathbf{I}_p) \mathbf{i}_k]^T [\mathbf{I}_p - \sum_{k=1}^{p-1} (\mathbf{i}_k^T \mathbf{I}_p) \mathbf{i}_k]}} \quad (3)$$

Any given interferogram, \mathbf{I}_s , may now be referenced to \mathbf{i}_p to provide an orthogonal vector, \mathbf{I}_{s-p} , given by

$$\mathbf{I}_{s-p} = \mathbf{I}_p - \sum_{k=1}^p (\mathbf{i}_k^T \mathbf{I}_s) \mathbf{i}_k \quad (4)$$

The magnitude of \mathbf{I}_{s-p} is the measure of radiation reduction due to absorption or other sampling effects in the interferogram. Thus, the "overall" absorbance of a spectrum compared to the typical background spectrum can be determined by a small number of calculations that avoid a Fourier transformation step. Since absorbance information in a spectral profile is incorporated into every interferogram element to a varying degree, the selection of a small, relevant region of the interferogram allows absorbance information to be obtained expeditiously.

Considerable discussion exists on the use of an appropriate region, or "window", of the interferogram for calculating the G-S basis set and intensity.¹⁰ In particular, the size and position of this window may be critical to the predictive performance of the technique. Various studies utilize regions away from the centerburst,^{10,11} while others stress the inclusion of the centerburst. The appropriate window for an experiment, which is chosen to maximize the signal-to-noise ratio (SNR), depends on the analytes and instrumentation^{10,11} and is usually chosen tens of points away from the centerburst.^{7,11} However, the region of the interferogram close to the centerburst, indicative of the transmitted intensity over the entire spectral bandwidth, is sensitive to both the total sample absorption and scattering effects.¹² Depending on the study parameters and absorption patterns of sample constituents, spectral window optimization methods may require inclusion of the centerburst.¹³ For IR spectroscopic imaging instruments, the scattering component in a spectrum provides an additional contrast variable across the field of view, similar to optical microscopy, in which the contrast is determined by differences in refractive indices between phases. Thus, spatial regions encompassing interfaces between sample phases of differing infrared refractive indices will demonstrate strong changes in the centerburst vicinity, while spatial regions away from the interface will be more sensitive to changes in the narrow-

er absorption bands, which arise from interferogram portions removed from the centerburst.

The size of the spectral window, or the number of specified interferogram points, defines the dimensionality of the basis set and depends on both the number of components and absorption patterns. Similarly, the number of interferograms employed for constructing the basis set requires optimization. A basis set must have a sufficient number of interferograms to be robust with respect to noise, but must contain as few interferograms as possible to maximize its discrimination ability and computation speed. The size and location of the interferogram window and the number of interferograms in the basis set depend on the number of constituent phases and require empirical determination as no "general" optimal conditions can be predicted.¹⁴ Since no more than six phases usually exist in an imaging data set, an empirical selection of 100 consecutive data points (out of 2048) displaced from the centerburst by 60 points and the use of a basis set of 60 suffices for segmentation.⁷ Using simultaneous simplex optimizations to improve prediction, a task computationally more expensive than a low-resolution fast Fourier transform (FFT) transformation, the number of basis vectors suggested was ~50–80% of the interferogram, including the centerburst.¹³ Another perspective on the region of the interferogram to be selected is afforded by an analysis of the contribution of the absorbance, $A\bar{\nu}$, at a wavenumber, $\bar{\nu}$, given by

$$\Delta I_s = - \int_{-\infty}^{\infty} B(\bar{\nu}) \left[\frac{A(\bar{\nu})}{\log_{10} e} \right] \cos(2\pi\bar{\nu}\delta + \theta_{\bar{\nu}}) d\bar{\nu} \quad (5)$$

where the retardation is denoted by δ , phase angle by $\theta_{\bar{\nu}}$ and spectral profile by $B(\bar{\nu})$. Clearly, the phase lag introduces a small shift in the maximum amplitude of the sample interferogram and inclusion of points close to the centerburst will sample the overall spectral profile as well as the wider bands in the system. In our application, the inclusion of the centerburst provides a region of high contrast in any image plane, and the larger signals around the centerburst are expected to provide enhanced SNR G-S profiles for stable interferometer performance. This advantage is not available for G-S profiles from macroscopic IR data in which the inclusion of the centerburst does not appreciably affect the SNR of the G-S profile.¹⁰ It must be noted that the image contrast resulting from including the centerburst originates from both absorption and scattering effects due to refractive index mismatches in a heterogeneous sample. Hence, we recommend excluding the centerburst when routinely performing G-S orthogonalization on heterogeneous samples in which spatial chemical differences are to be determined and including it only when *any* difference is critical to the task, as for example, in quality control applications.

EXPERIMENTAL

Instrumentation. The instrumentation consists of a research-grade step-scan spectrometer (Bruker IFS 66/s) attached to an IR microscope (Bruker IR Scope II). The microscope, employing all-reflective Cassegrainian focusing optics consisting of a 15× objective lens and a 10× condensing optic, contains a 256 × 256 element mercury cadmium telluride (MCT) focal plane array, or

FPA (Santa Barbara Focalplane, CA), at the distal end of the optical train. The optical magnification and pixel size of the FPA results in a nominal spatial resolution of $\sim 3 \mu\text{m}$. A single interferogram is acquired for every pixel in the imaging configuration and the entire data set consists of 65 536 interferograms. The FPA contains an optimized cold shield and a long-wavelength bandpass filter ($3950\text{--}0 \text{ cm}^{-1}$) to prevent stray radiation and aliasing, respectively. For time-resolved experiments involving liquid crystalline microdomains, event-locked signal generators (Agilent Inc.) are employed to initiate data acquisition and sample excitation. A commercially available amplifier (Krohn-Hite Corp.) is employed to increase the electrical potential difference generated (5 V at 2 KHz) by a gain factor of 5 before being applied to the sample. Signal magnitudes and timing were verified using a digital oscilloscope (Tektronics Inc. model TDS 224).

Sample. Two samples, spanning the biological and materials science disciplines, were selected. The first represents a skin sample that had been rapidly frozen, embedded in a cutting medium and sectioned to a $10 \mu\text{m}$ thickness. The sample was first washed repeatedly with an ethanol solution diluted in water to remove the embedding medium and then mounted on a BaF_2 optical crystal. The polymer sample reflects a phase-separated blend consisting of poly(isobutyl methacrylate) [PiBMA], of an average molecular weight equal to 130 000 (Aldrich Corp.), and a eutectic liquid crystal mixture, E7 (EM Industries, Inc.); these materials were used as received. Ratios of the starting materials were dissolved in methyl isobutyl ketone (MIBK) to obtain an approximately 1% solution, which was subsequently employed to cast thin films of the blend on germanium substrates. The blend film was dried in air for three days, followed by heating in an oven at $\sim 120 \text{ }^\circ\text{C}$. A second germanium window, employed to provide the second electrode to the film, was separated from the blend containing substrate by $10 \mu\text{m}$ diameter cylindrical fiberglass spacers. Constant film thickness was attained by heating ($80 \text{ }^\circ\text{C}$) under pressure.

Experimental Parameters. For the imaging experiments, interferogram data points are acquired at every fourth zero crossing of the He-Ne laser to limit the acquired data spectral range ($3950\text{--}0 \text{ cm}^{-1}$) to within the detection range of the FPA and to reduce the size of the data set. The resulting interferograms, consisting of 1024 points each, are zero filled by a factor of two and fast Fourier transformed to provide single beam spectra with a nominal spectral resolution of 8 cm^{-1} and $3950\text{--}0 \text{ cm}^{-1}$ spectral range. For time-resolved spectroscopy (TRS) experiments, the sample was excited once every 5 s, resulting in a data collection time of $\sim 5100 \text{ s}$ per interferogram acquisition. The maximum frame rate of the focal plane array is $\sim 114 \text{ Hz}$, allowing a duty cycle where the FPA acquires data once every 10 ms (100 Hz). All data processing software is written in-house using IDL/ENVI (RSI Inc.) and calculations are performed on a standard desktop PC.

RESULTS AND DISCUSSION

Application to a Static Biological Sample. Figure 1 illustrates G-S orthogonalization for interferograms from

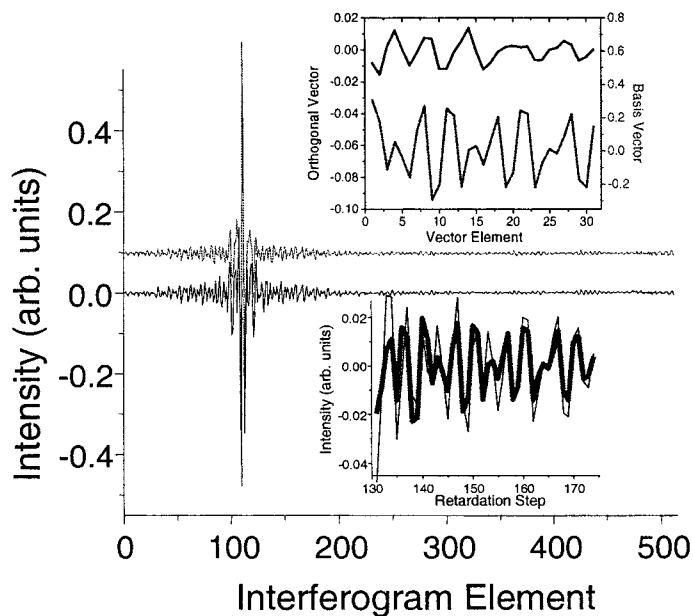


Fig. 1. Typical interferograms from the background (light line, offset by 0.1 units) and sample of human skin tissue (dark line), respectively. The inset at the bottom shows the difference in the interferogram intensity for the sample and the background denoted by the thin and thick lines, respectively. The inset at the top shows the basis vector for a region (bottom curve, right axis) of the interferogram derived from the background and the corresponding orthogonal vector of the sample derived from the sample interferogram (top curve, left axis).

a randomly selected pixel for the background and sample of human skin tissue. Differences in interferogram intensity can be observed for a small region of the interferogram as shown in the lower inset. The typical root mean square (rms) noise, measured by subtracting sequentially acquired interferograms, is of the order of 0.0002 arbitrary units. The basis vector set and the corresponding orthogonal vectors are shown in the upper inset. The intensity of the orthogonal vector is close to zero for similar intensity regions in the interferograms. Based on the addition of noise for a 30-element vector when the magnitude is calculated, the signal-to-noise ratio of the typical G-S intensity should be, at least, ~ 100 . The actual value will depend on the intensity of individual elements and the size of the orthogonal vector, but the orthogonalization can be expected to result in an error whose magnitude is $\sim 1\text{--}10\%$, which is reasonable for the effort expended in extracting information.

An infrared brightfield image of the sample, represented by the amplitude of the interferogram centerburst, is shown in Fig. 2a. The centerburst amplitude measures the recorded throughput and depends on the initial illumination, substrates, refractive indices, and scattering properties of the sample, as well as the spectral absorbance, which is the principal quantity of interest. Although the instrument has been optimized and the sample illumination is uniform, it becomes difficult to identify individual contributions. Thickness variations, for example, could lead to higher absorbance values that reduce the centerburst magnitude; scattering due to refractive index mismatches within the heterogeneous sample also leads to analogous problems. Areas of high intensity in the brightfield image indicate a region of high transmis-

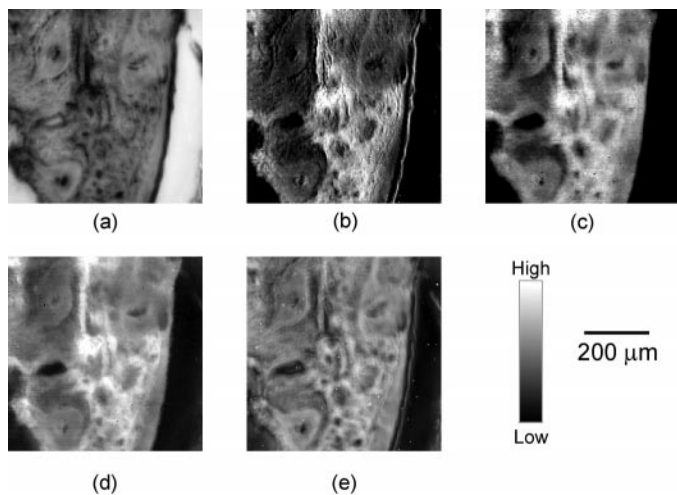


FIG. 2. (a) Infrared brightfield image, (b) nucleic acid–amide III absorbance area ($1120\text{--}980\text{ cm}^{-1}$) corresponding to the absorbance features, (c) amide II absorbance area ($1592\text{--}1480\text{ cm}^{-1}$), (d) OH–NH absorbance area ($3670\text{--}3130\text{ cm}^{-1}$), and (e) orthogonalized G-S intensity images for a human skin tissue sample. The intensity grayscale denotes regions of low intensity by shades closer to black and those of high intensity closer to white for photon flux in the brightfield image in (a), for the absorbance magnitude for modes described in (b–d), and for the G-S intensities in (e).

sion or lack of sample. The imaging data set of the sample is then transformed to provide spectral absorbance intensities over the field of view. Figures 2b through 2d show the spatial intensity distribution of specific spectral absorbance features. The spectral absorbance from any pixel is a function of both the chemical content reflected by the pixel position and the local sample thickness. Areas of high absorbance are indicated by lighter grayscale values, while areas reflecting low absorbance values are indicated by shades close to black, thus highlighting the complementary nature of the brightfield and absorbance images. The G-S intensity, calculated using 40 interferogram points starting 20 points away from the centerburst, are plotted in a manner similar to an absorbance plot to obtain the image shown in Fig. 2e.

The orthogonalized G-S intensity image in Fig. 2e reflects the characteristic spatial features present in the three specific absorbance images (Figs. 2b–2c). While characteristic features due to the absorbance of specific vibrational modes are not reproduced explicitly, the contrast in the G-S intensity image is sufficiently indicative of the various spatial features illustrated in the absorbance images. In particular, it must be noted that only the absorbance image of the amide III–nucleic acid complex ($1320\text{--}1160\text{ cm}^{-1}$ area) in Fig. 2b shows the presence of a multilayer structure in the tissue towards the right that is clearly reproduced only by the G-S image. In a similar manner, residual debris from the cutting medium, which consists of polyglycols, next to the tissue, is apparent only in the NH–OH stretching area ($3700\text{--}3050\text{ cm}^{-1}$) absorbance and the G-S intensity images. Similarly, it may be argued that the contrast in the G-S intensity image appears greater than that obtained by plotting the absorbance alone of the amide II peak (Fig. 2c). While the detailed molecular composition information is lost in a composite figure given by the G-S inten-

sity, visualization is still based on absorbance and provides remarkable spatial contrast.

Many imaging data sets are acquired from samples containing air–sample interfaces that leave a fraction of the image without any data from the sample. G-S intensity data can be readily employed to delineate these regions. For example, for the skin sample above, the areas that do not contain an appreciable thickness of tissue will not provide a good signal for biomedical analyses. Typically, absorbance spectra are calculated for all pixels in an imaging data set, and the pixels that do not contain sufficient tissue to provide a signal three times larger than noise, which is a commonly accepted detection limit, are excluded from subsequent analysis. G-S intensity values may be employed for the same task of masking these low-signal pixels. Just as selection of an absorbance mode is not trivial for the task, selection of a cut-off G-S intensity is not universal and depends on the selected processing parameters, such as the interferogram window and the experimental variables, including atmospheric effects and instrument drift, that are employed. Hence, care must be exercised when determining sample regions for examination. In the reported examples, and experience with other data sets, the G-S vector intensities for pixels not containing sample were 2–3 orders of magnitude smaller than sample pixels, making the G-S vector intensity an excellent indicator of spatial regions that did not contain samples. In control applications, where identical samples are employed repeatedly, the acceptance threshold can be determined *a priori* and easily incorporated in any analysis algorithm.

Application to Dynamic Imaging Data. PDLCs are a class of polymer composites whose optical properties are changed by application of an electrical potential. An absorbance image of a liquid crystalline (LC) specific vibrational mode, demonstrating LC-rich domains in a PDLC, is shown in Fig. 3a. When an electric field is applied, liquid crystal molecules in the LC-rich domains experience a reorientational torque and align along the direction of the electric field, which is perpendicular to the electric vector of the IR beam propagating in the direction of the applied potential difference. Upon reorientation, molecular moieties whose transition moments align with the direction of IR beam propagation undergo a decreased absorbance. Time-resolved FT-IR spectroscopic imaging is employed to observe this dynamic behavior of the LC domains *in situ*. Given that the process needs to be monitored using tens of temporal measurements, a data set for a time-resolved experiment is typically several gigabytes in size. For example, the data set analyzed here requires 12.5 GB of storage. The processing of such large data sets to yield absorbance profiles requires several hours.

The G-S intensity, however, can be obtained, as before, for every temporal resolution element data set to construct a profile of the G-S intensity as a function of time. By employing a subset of the time-resolved data to calculate the basis vectors, changes in absorbance from this quiescent state can be easily monitored. We extract average temporal profiles of the G-S intensity from pixels in two microdomains of a PDLC, shown in Fig. 3b, where the white pixels in the figure of the droplet can be unambiguously assigned to the microdomains. The two

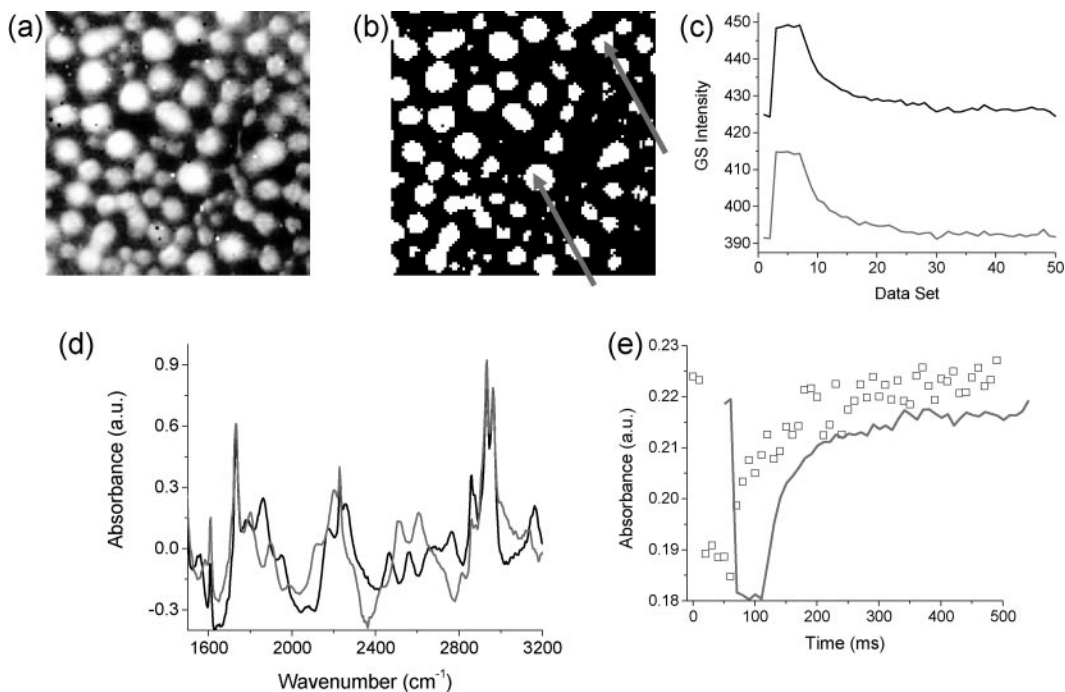


FIG. 3. A polymer-dispersed liquid crystal sample demonstrating (a) the spatial absorbance distribution of the nitrile vibrational mode at 2227 cm^{-1} . (b) Liquid crystal rich domains are delineated and average profiles from two droplets, as indicated, are employed to plot (c) G-S intensities as a function of the data set number, (d) a section of average absorbance spectra, and (e) an overlay absorbance profile (open squares) and processed G-S intensity (solid line).

extracted G-S profiles, shown in Fig. 3c, demonstrate the same general features. Large interference fringes are present in absorbance spectra, shown in Fig. 3d, due to the reflective properties of the substrate and the constant thickness of the cell. This distorting feature is present in the recorded interferograms as a sharp spike close to the centerburst. By calculating G-S vectors utilizing points distant from these spikes, distortion-free temporal profiles are obtained. Residual substrate effects combined with differences in optical properties of the two domains, when compared to the background interferogram, introduce differences in the absolute values of the G-S intensities. Qualitatively, however, the two profiles are very similar, demonstrating, as expected, that the temporal behavior of the two domains is similar.

Irrespective of whether the absorbance increases or decreases, the G-S intensity, being a vector magnitude, shows a positive deviation upon change in absorbance. To achieve correspondence with a temporal absorbance profile demonstrating a decrease, the G-S intensity can be inverted and scaled to resemble the variation of the spectral absorbance. A comparison of the G-S intensity profile processed in this manner and the absorbance from a liquid crystal specific vibrational mode is shown in Fig. 3e. The agreement between the two profiles is quite good. In this case, the G-S intensity profile is less noisy than the absorbance profile due to the inherent advantage of the G-S process in utilizing a small, low-noise portion of the interferogram and avoiding the effects of the absorbance fringe pattern. In general, no *a priori* method may be suggested for extracting G-S intensities to reproduce features observed in absorbance spectra. Reasonable absorbance features, however, can be reproduced very rapidly and, as shown above, several absorbance artifacts are

avoided by using G-S orthogonalization for preliminary data processing.

Effects of Noise, Detection Limits, and Computation Efficiency. Noise in G-S profiles arises from detector noise, noise outside the spectral bandwidth, and from instabilities in spectrometer performance. In general, we have implemented a highly stable sampling scheme employing high-quality electronics constructed in-house, coupled to a research-grade interferometer. A measurement of successive interferograms confirms that there is little difference between the noise at the centerburst and in the wings. However, the instrument is subject to slow drift and changes in atmosphere over the time of the experiment. Slight interferometer instability, which cannot be readily differentiated from $1/f$ noise in the system, may contribute to the noise observed in the G-S profiles. Phase errors are considered negligible in our analysis but are usually not negligible for spectral data acquired in the configuration reported here, as can be observed from the slight chirping in the interferograms in Fig. 1. The phase angle, however, is a slowly varying function of the wavenumber and can be accounted for by a small region of the interferogram around the centerburst, precluding the effects of phase when a particular interferogram region away from the central region is selected for calculating G-S intensities. Pixel-to-pixel variations are expected to be very small as the G-S orthogonalization is carried out on the same pixel and does not affect any other pixel.

Gram-Schmidt orthogonalization, as implemented here, is one of the most efficient orthogonalization methods.¹⁵ Specifically, the number of operations⁷ to form the basis is $2D(2p + 1) + 1$, while the number of operations for subsequent orthogonalizations is $D(4p - 1)$, where D is the number of dimensions or vector elements and p is

the number of vectors. Using an FFT algorithm for a discretely sampled interferogram of N elements, the number of corresponding operations is of the order of $2N \log_2 N$. For a 1024 element interferogram employed for the imaging data set, where 30 points are employed for calculating the basis and orthogonal vectors from single files, the relative number of computations is ~ 20480 to 331. This ratio of number of computations is typically of the order of 1–5%; thus, considerable computational time savings are realized. In the example of imaging data, the time required to obtain a G-S intensity profile is approximately 2 minutes, while the time required to obtain an absorbance profile, which includes Fourier transformation, conversion to absorbance format, and calculation of the absorbance profile, required over two hours.

CONCLUSION

Gram–Schmidt vector procedures for imaging data analyses produce useful visualizations for both static and dynamic spectroscopic imaging data while being faster than the usual method of Fourier transformation followed by absorbance calculations. G-S orthogonalization requires neither an *a priori* knowledge of the constituents of a multiphase system nor that all sample components have unique and distinct spectral bands for segmentation purposes. The quantitative correlation of absolute GC intensities to concentration or absorbance may, however, be complicated by the presence of multiple components and the large absorbance and optical effects that are convo-

luted within the interferogram. Given the small number of computations and the need for only a limited portion of the interferogram, G-S processing can provide visualizations of spectroscopic imaging data in real time. We anticipate that this approach can be employed to routinely visualize spatial structure during data acquisition and is specifically suited for use in quality and process control applications.

1. E. N. Lewis, P. J. Treado, R. C. Reeder, G. M. Story, A. E. Dowrey, C. Marcott, and I. W. Levin, *Anal. Chem.* **67**, 3377 (1995).
2. R. Bhargava and I. W. Levin, *Anal. Chem.* **73**, 5157 (2001).
3. J. M. Chalmers, N. J. Everall, K. Hewitson, M. A. Chesters, M. Pearson, A. Grady, and B. Ruzicka, *Analyst* (Cambridge, U.K.) **123**, 579 (1998).
4. R. J. Hendershot, P. T. Fanson, C. M. Snively, and J. A. Lauterbach, *Angew. Chem., Int. Ed. Engl.* **42**, 1152 (2003).
5. R. Bhargava and I. W. Levin, *Appl. Spectrosc.* **57**, 357 (2003).
6. G. B. Arfken, H.-J. Weber, Eds., in *Mathematical Methods for Physicists* (Harcourt, New York, 2000), 5th ed., p. 596.
7. J. A. DeHaseh and T. L. Isenhour, *Anal. Chem.* **49**, 1977 (1977).
8. F. Cadet and B. Offman *Spectrosc. Lett.* **29**, 910 (1996).
9. H. Soltanian-Zadeh, J. P. Windham, and A. E. Yagle, *IEEE Trans. Nucl. Sci.* **40**, 1204 (1993).
10. G. M. Brissey, D. E. Henry, G. N. Giss, P. W. Yang, P. R. Griffiths, and C. L. Wilkins, *Anal. Chem.* **56**, 2002 (1984).
11. D. T. Sparks, R. B. Lam, and T. L. Isenhour, *Anal. Chem.* **54**, 1922 (1982).
12. R. Bhargava, S. Q. Wang, and J. L. Koenig, *Appl. Spectrosc.* **52**, 323 (1998).
13. R. L. White, G. N. Giss, G. M. Brissey, and C. L. Wilkins, *Anal. Chem.* **53**, 1778 (1981).
14. R. L. White, G. N. Giss, G. M. Brissey, and C. L. Wilkins, *Anal. Chem.* **55**, 998 (1983).
15. S. M. Donahue and C. W. Brown, *Anal. Chem.* **63**, 980 (1991).